Supporting Information

A Distinctive Conversion Mechanism for Reversible Zinc Ion Storage

*Yandong Ma,[a] Yuruo Qi, *[a] Yubin Niu, [a] Yijun Liu, [a] Shujuan Bao, [a] and Maowen Xu*[a]*

[a] Chongqing Key Lab for Advanced Materials and Clean Energies of Technologies, School of Materials and Energy, Southwest University, Chongqing, 400715, P.R. China.

Experimental Procedures

Preparation of V_2O_3@C

V_2O_3@C was prepared by a simple one-step carbothermal reduction strategy. 1.0 g NH_4VO_3 (AR, Aladdin) was mixed and ground with a few drops of deionized water, then mix the grinding solution with 10 ml 1M HCl (36%-38%. wt%, Chongqing Chuandong Chemical Group Co., Ltd.) solution under continuous stirring, and the milky white liquid immediately turns red. Subsequently, deionized water was added to a total volume of 20 ml, stirred for a few minutes to complete the reaction, and let stand to precipitate the red reaction product. After removing the supernatant, add water to 20 ml again, and in a water bath at 90°C for a few minutes with vigorous stirring, then the supernatant was removed. This process was repeated three times, and finally water was added to 40 ml to obtain a homogeneous $V_2O_5 \cdot nH_2O$ dispersion.

Subsequently, 40μL of aniline (Aladdin, used after purification by distillation under reduced pressure.) monomer was dispersed in 100ml of deionized water, and then the obtained $V_2O_5 \cdot nH_2O$ dispersion was transferred to the aniline solution. The red reactant quickly turned dark green, which indicates that the aniline was chemical oxidized and polymerized in $V_2O_5 \cdot nH_2O$ in situ. On the surface, a polyaniline-

coated $V_2O_5 \cdot nH_2O$ structure is formed (PVOH). Next, the reaction product was freeze-dried, and heat-treated under an argon atmosphere at 680°C for 2 hours. The carbon skeleton obtained by carbonization of polyaniline is employed as reducing agent to obtain carbon-coated V_2O_3 (V_2O_3@C).

Characterization of materials

The ex-situ X-ray diffraction (XRD) pattern of the prepared material and electrode material was measured by a powder X-ray diffraction system (XRD, Shimdzu XRD-7000) using Cu Kα radiation (40 kV, λ=0.15418 nm). Observe the microscopic morphology and structural characteristics of the sample by field emission scanning electron microscope (FESEM, JSM-7800F, Japan) and transmission electron microscope (TEM, JEM-2100, Japan). X-ray photoelectron spectroscopy (XPS) was performed in a Thermo Scientific ESCALAB 250Xi electron spectrometer to construe the constituent of the samples. The JWGB surface area and porosity analyzer is employed to study the pore structure. The specific surface area is analyzed by Brunauer-Emmett-Teller (BET) theory. The pore size distribution (PSD) is calculated according to the Barret-Joyner-Halenda (BJH) model. Calculate the total pore volume from the adsorption capacity at a relative pressure P/P0 of 0.99.

Electrochemical characterization

The prepared V_2O_3@C sample was mixed with acetylene black and polyvinylidene fluoride (PVDF) at a ratio of 7:2:1, and an appropriate amount of nitrogen methyl pyrrolidone (NMP, AR, Aladdin) was added dropwise and then ground to form a uniform conductive slurry. Then, it was knife-coated on the titanium foil and dried in an oven at 60° C to prepare a positive electrode. The Zn (99.99%) negative electrode has not undergone any treatment. Zinc trifluoromethanesulfonate (Aladdin) is used as an electrolyte, with the concentration of 3M in aqueous and glass fiber filter (Whatman, Grade GF/A) as the separator. All button batteries (CR-2032 type) are assembled in an air atmosphere. The cyclic voltammetry curve was tested using Shanghai Chenhua Electrochemical Workstation (CHI660E), and electrochemical impedance spectroscopy was tested in the frequency range from 0.01 Hz to 100 kHz on Autolab workstation (AUT87168). The galvanostatic charge–discharge was obtained on a LAND CT2001 test system (Wuhan LAND electronics Co., Ltd, China).

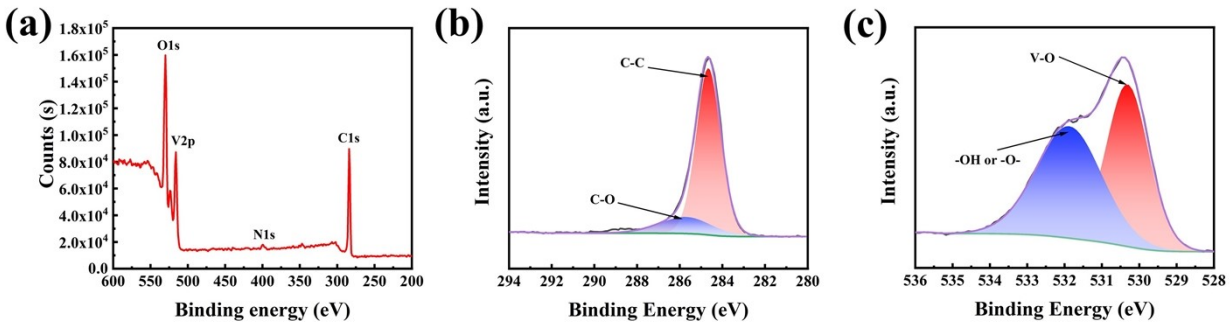

Figure S1. (a) XPS spectrum of V_2O_3@C. High resolution XPS spectra of (b) C *1s*, and (c) O *1s*.

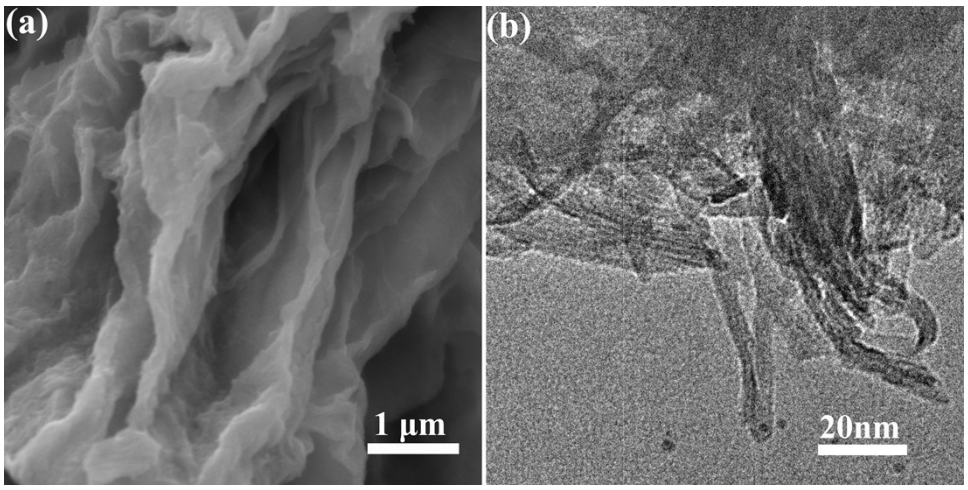

Figure S2. (a) the FE-SEM and (b) the TEM images of precursor PVOH.

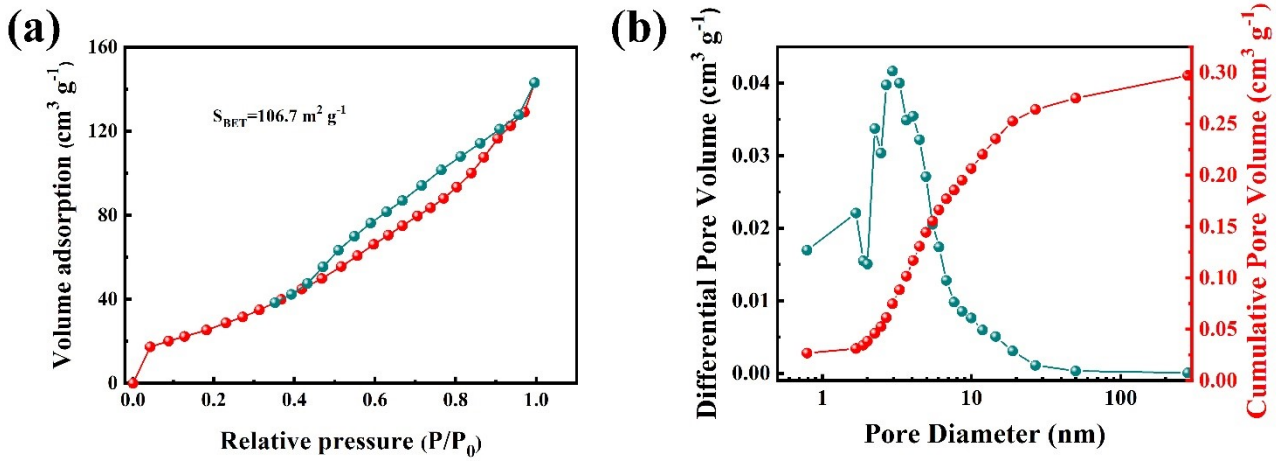

Figure S3. (a) Nitrogen adsorption/desorption isotherm and (b) corresponding pore size distribution.

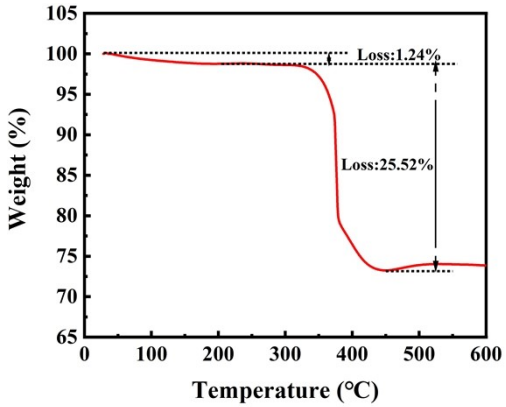

Figure S4. TGA curve of V_2O_3@C.

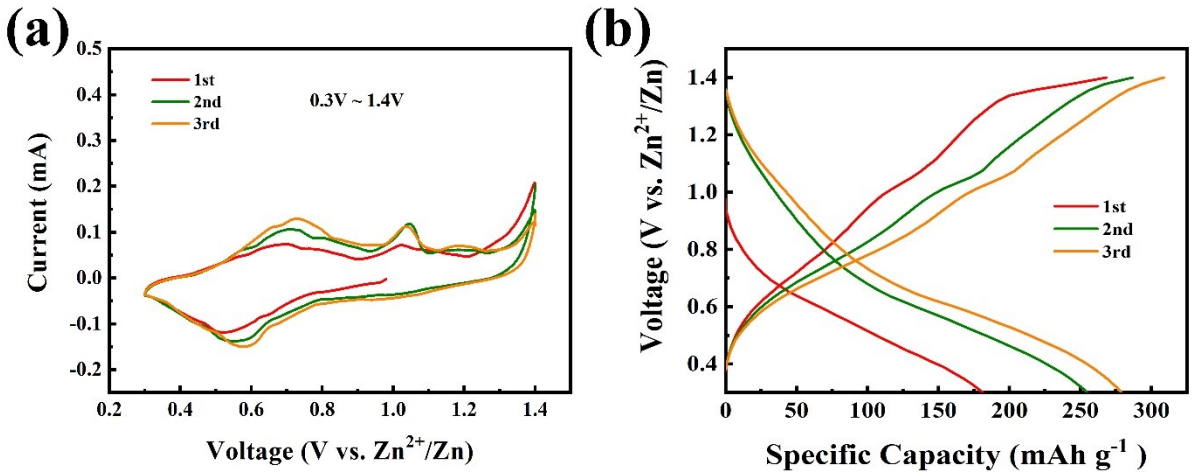

Figure S5. Unusual charging behavior of V_2O_3@C. (a) CV curves with the scan rate of 0.1 mV s^{-1} in 0.3 - 1.4 V, and (b) GCD curves at 0.1 A g^{-1} with the voltage range of 0.3 - 1.4 V.

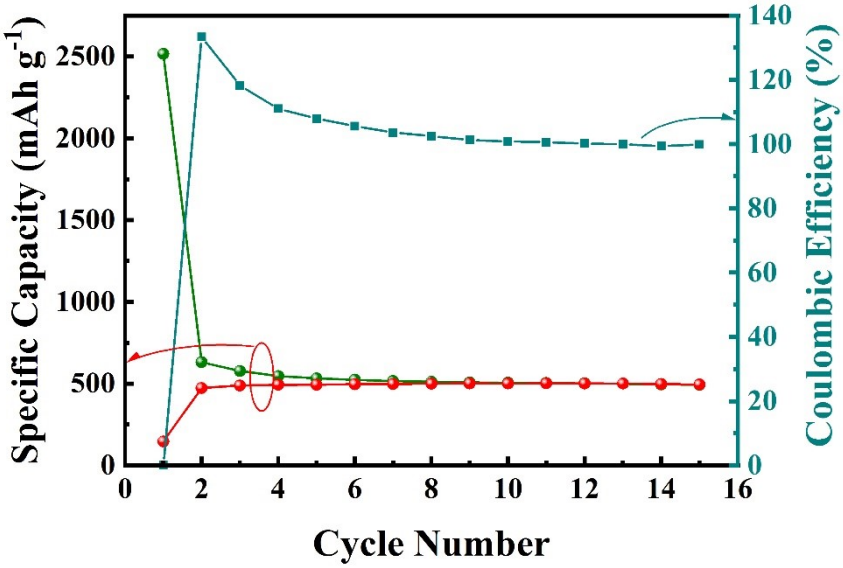

Figure S6. The performance of the first 15 cycles at the current density of 0.1 A g^{-1}.

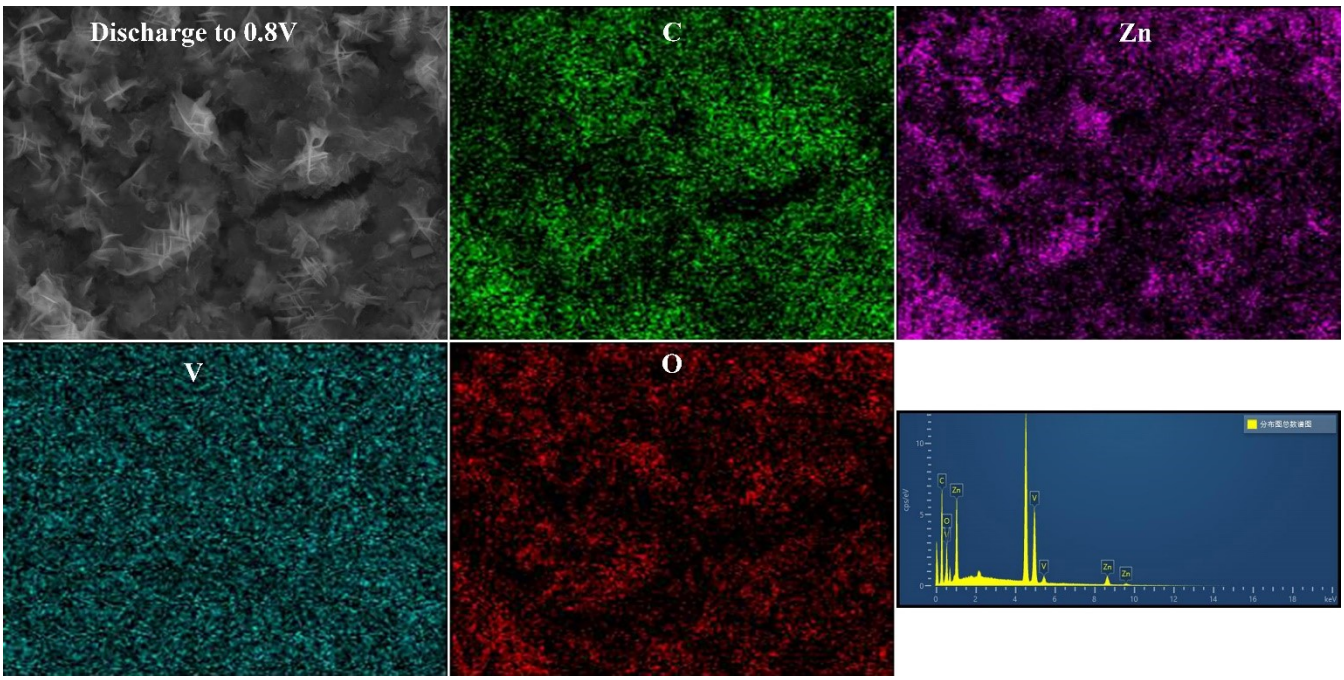

Figure S7. EDS mapping when discharged to 0.8V.

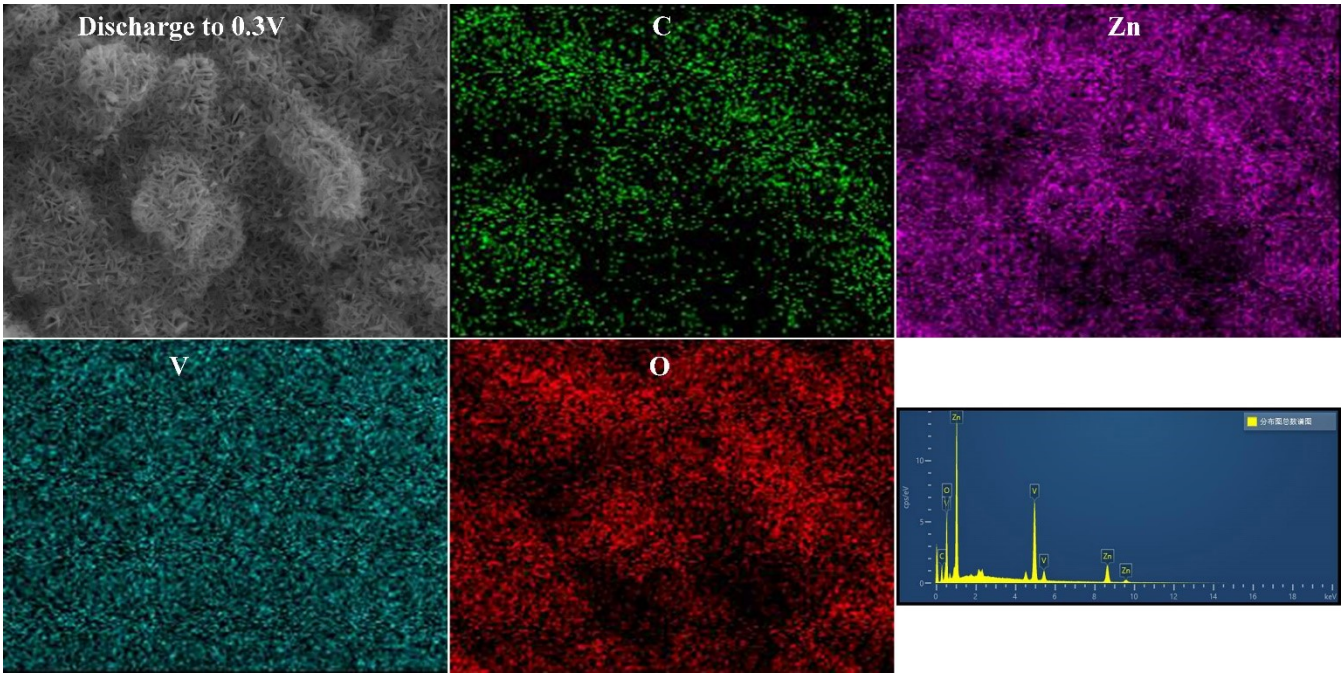

Figure S8. EDS mapping when discharged to 0.3V.

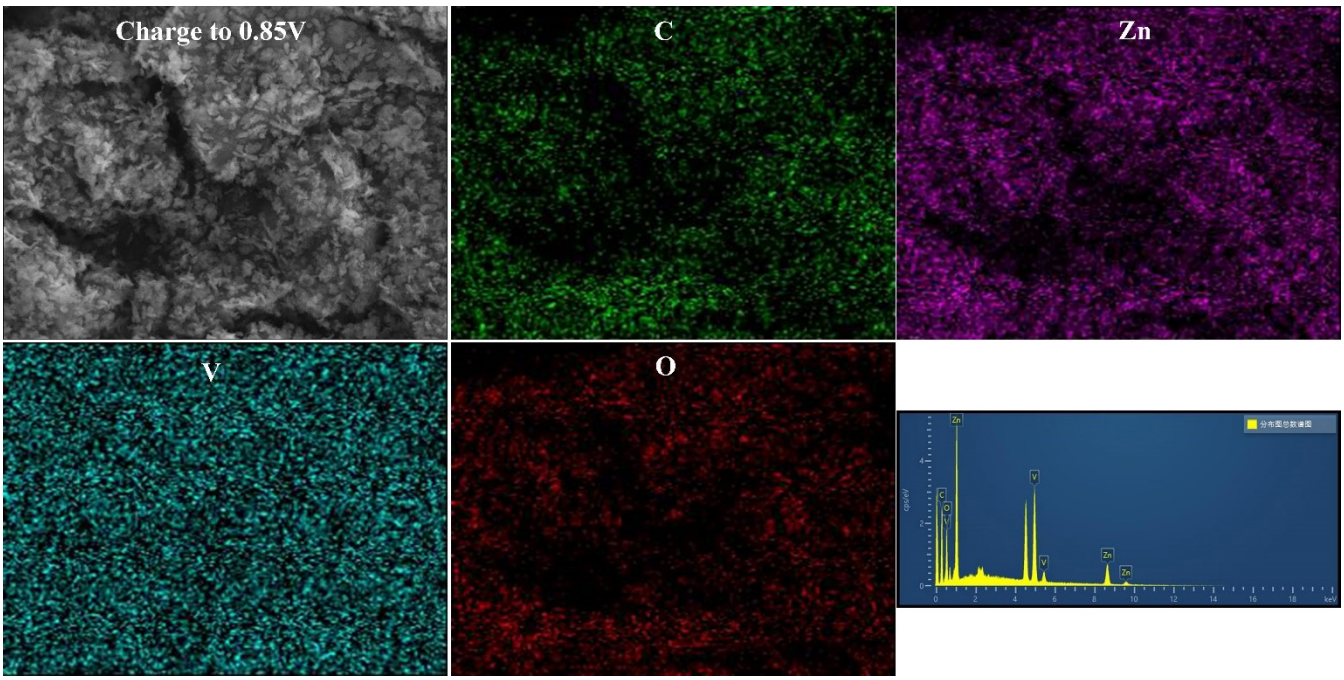

Figure S9. EDS mapping when charged to 0.85V.

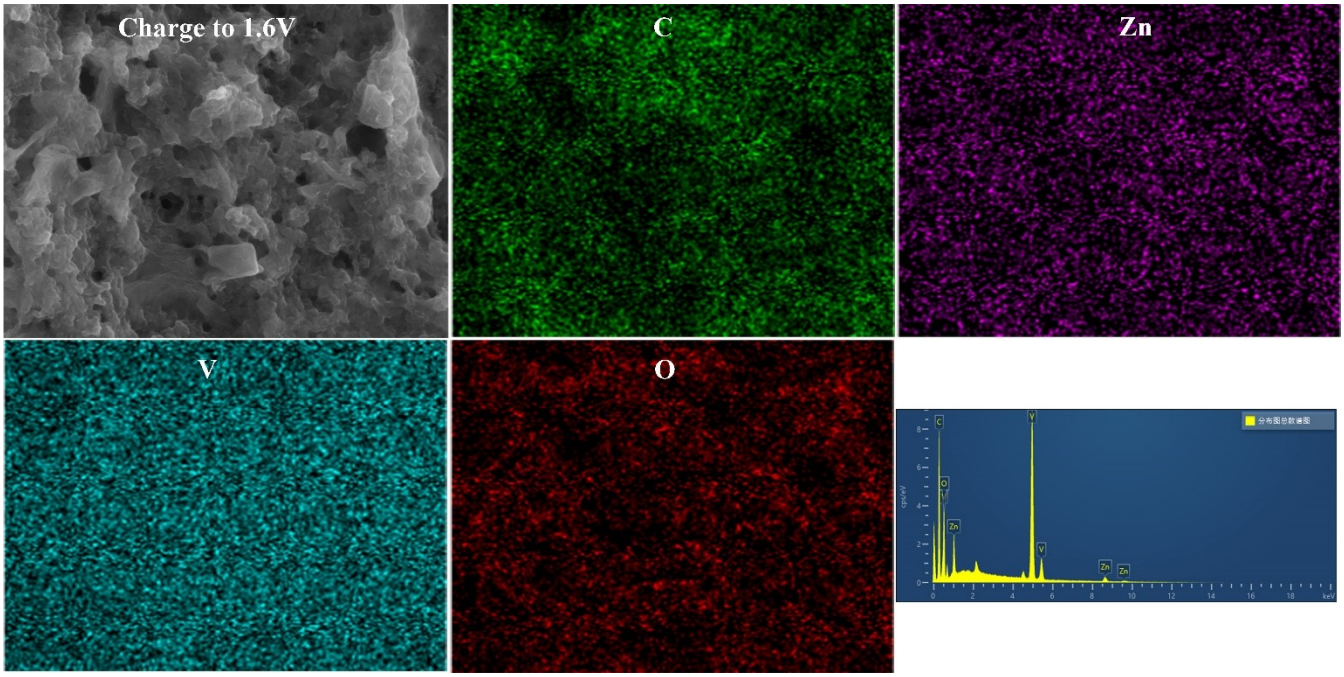

Figure S10. EDS mapping when charged to 1.6V.

Table S1. The element content based on EDS mapping.

	C (%)	Zn (%)	V (%)	O (%)
Discharge to 0.8V	67.65	4.99	9.54	17.82
Discharge to 0.3V	28.74	16.23	16.80	38.22
Charge to 0.85V	59.62	8.53	10.74	21.11
Charge to 1.6V	61.79	1.82	14.89	21.51

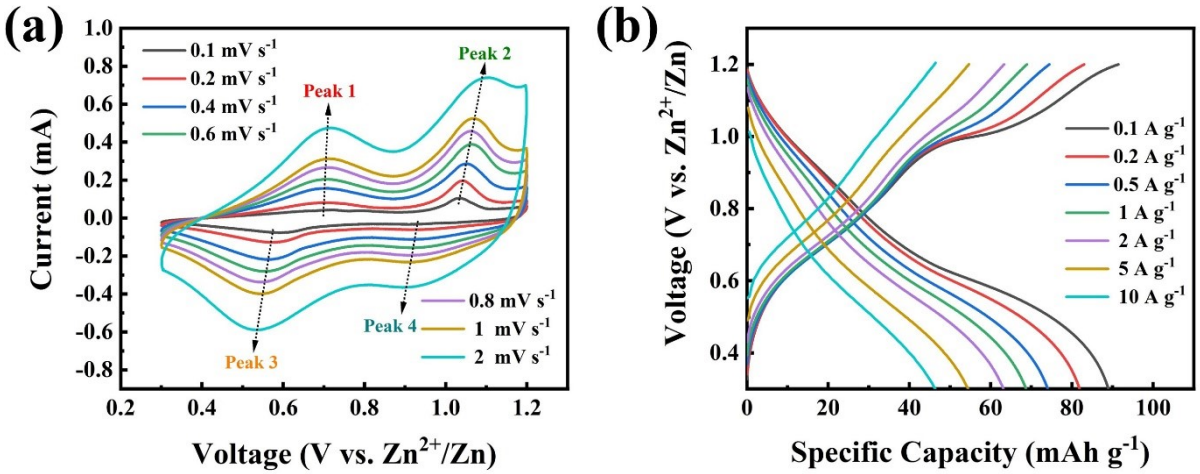

Figure S11. (a) CV curves with different scan rates and (b) GCD curves with different current densities at 0.3-1.2 V.

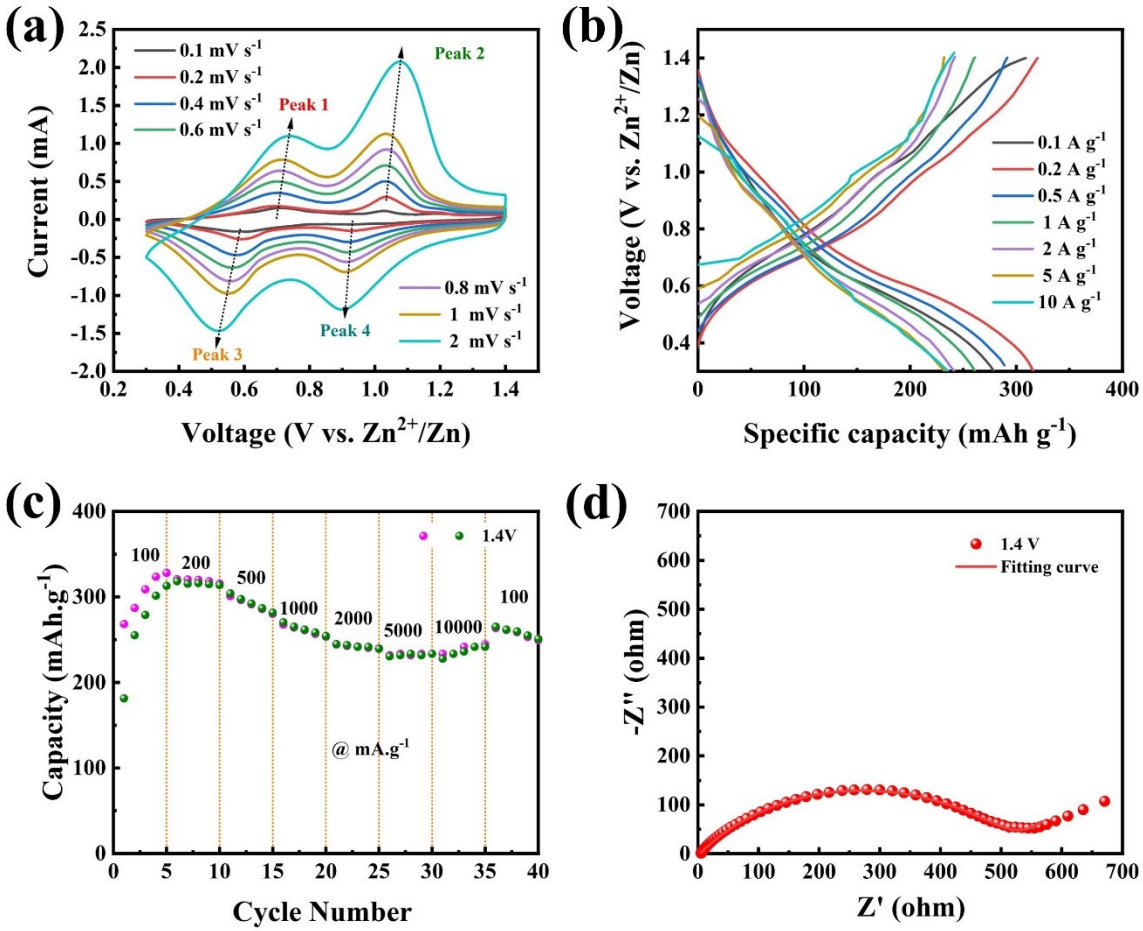

Figure S12. (a) CV curves with different scan rates, (b) GCD curves with different current densities, (c) rate performance and (d) EIS at 0.3-1.4 V.

The CV curves at 1.2 V and 1.4 V were also compared, as shown in Figures S11a and Figure S12a. Obviously, the CV curves cover a larger area in the voltage range of 0.3-1.4 V, which means a higher specific capacity. And the GCD curves (Figures S11b and Figure S12b) further confirm this conclusion due to the partial oxidation of V_2O_3. Nevertheless, it is far lower than the electrochemical performance at 1.6 V (Figure 3b and Figure S10c).

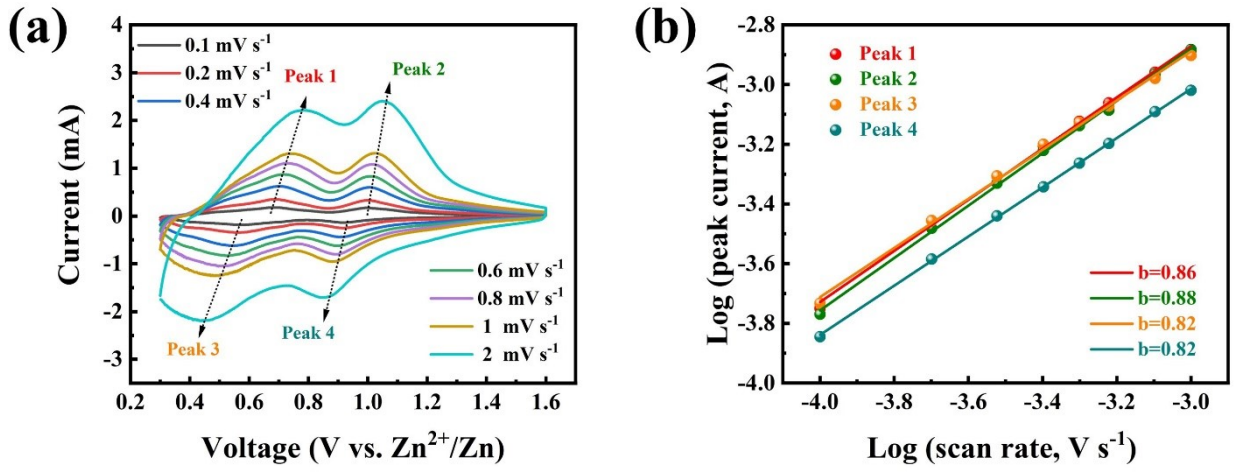

Figure S13. (a) CV curves of V_2O_3@C at different scan rates and (b) The relationship between peak currents and scan rates.

The peak current is statistically introduced to calculate the value of b according to the formula[1, 2]:

$$i = av^b \qquad (1)$$

Where i is peak current, v is the scan rate, a and b are adjustable parameters.

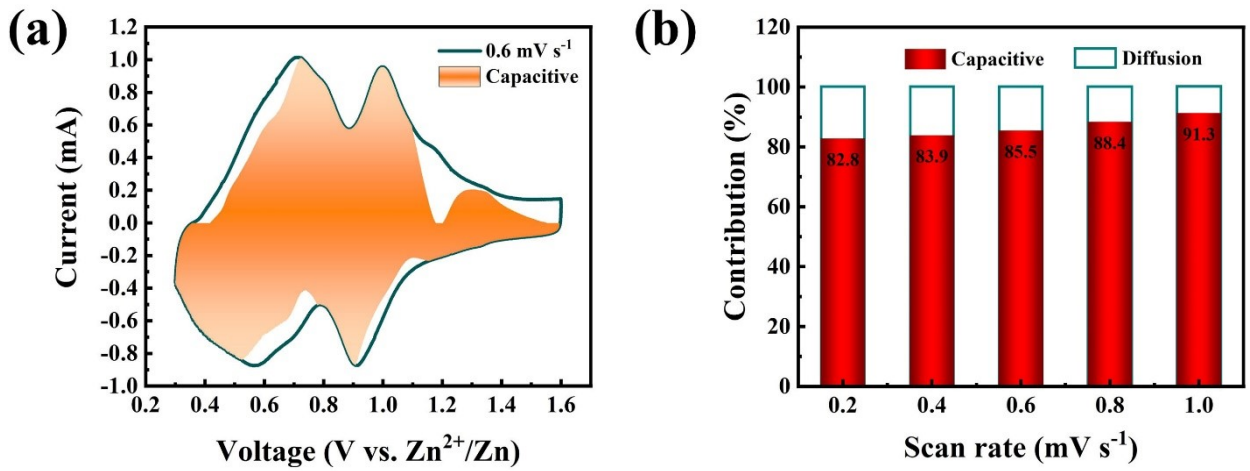

Figure S14. (a) Capacitive contribution at 0.6 mV s^{-1} (85.5%) and (b) The percentages of capacitive and diffusion contributions at different scan rates.

The capacitance response and diffusion process are quantified by the following formula[3, 4]:

$$i = k_1 v + k_2 v^{1/2} \qquad (2)$$

In which k_1 and k_2 are constants at a specific scan rate, and v and i are the scan rate and the corresponding peak current, respectively.

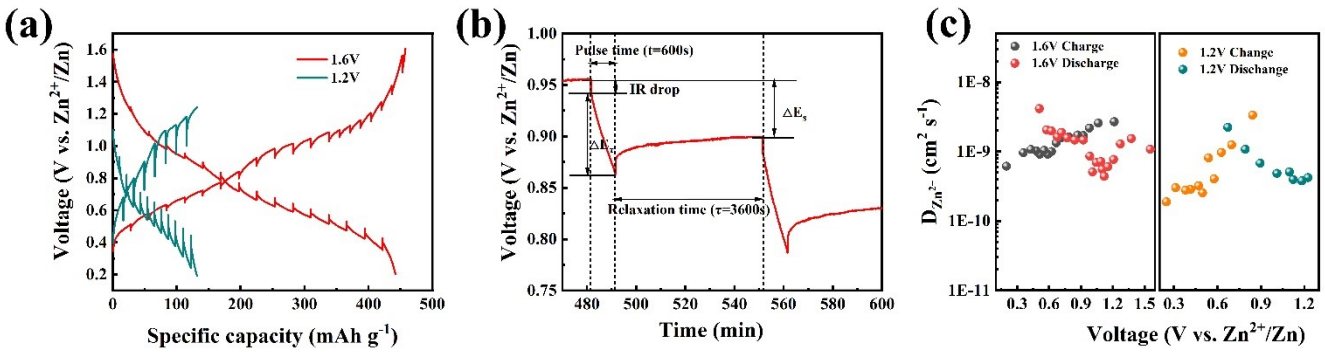

Figure S15. (a) GITT tests at the current density of 0.1 A g^{-1}, (b) Schematic illustration of a GITT measurement signal step during the discharge process and (c) Corresponding ion diffusion coefficients.

The GITT was employed to calculate the ion diffusion coefficient of Zn^{2+} based on the following equation[5-7]:

$$D_{Zn^{2+}} = \frac{4}{\pi\tau}\left(\frac{m_B V_M}{M_B S}\right)^2 \left(\frac{\Delta E_s}{\Delta E_\tau}\right)^2 \quad (3)$$

where τ is the duration time of the current pulse (3600s), m_B is the mass of the active materials, V_M is the molar volume ($cm^3\ mol^{-1}$), M_B is the molecular weight ($g\ mol^{-1}$), S is the total contacting area of electrode with electrolyte, and ΔE_s and ΔE_τ are related to the change of steady-state voltage and overall cell voltage for the corresponding step.

References

1. D. Bin, W. Huo, Y. Yuan, J. Huang, Y. Liu, Y. Zhang, F. Dong, Y. Wang and Y. Xia, Organic-Inorganic-Induced Polymer Intercalation into Layered Composites for Aqueous Zinc-Ion Battery, *Chem*, 2020, **6**, 968-984.
2. D. Yu, Z. Wei, X. Zhang, Y. Zeng, C. Wang, G. Chen, Z. X. Shen and F. Du, Boosting Zn^{2+} and NH^{4+} Storage in Aqueous Media via In-Situ Electrochemical Induced VS_2/VO_x Heterostructures, *Advanced Functional Materials*, 2021, **31**, 2008743.
3. S. Li, Y. Liu, X. Zhao, Q. Shen, W. Zhao, Q. Tan, N. Zhang, P. Li, L. Jiao and X. Qu, Sandwich-Like Heterostructures of MoS_2/Graphene with Enlarged Interlayer Spacing and Enhanced Hydrophilicity as High-Performance Cathodes for Aqueous Zinc-Ion Batteries, *Advanced Materials*, 2021, **33**, 2007480.
4. J. Ding, H. Zheng, H. Gao, Q. Liu, Z. Hu, L. Han, S. Wang, S. Wu, S. Fang and S. Chou, In Situ Lattice Tunnel Distortion of Vanadium Trioxide for Enhancing Zinc Ion Storage, *Advanced Energy Materials*, 2021, **n/a**, 2100973.
5. H. Luo, B. Wang, F. Wu, J. Jian, K. Yang, F. Jin, B. Cong, Y. Ning, Y. Zhou, D. Wang, H. Liu and S. Dou, Synergistic nanostructure and heterointerface design propelled ultra-efficient in-situ self-transformation of zinc-ion battery cathodes with favorable kinetics, *Nano Energy*, 2021, **81**, 105601.
6. Z. Yao, Q. Wu, K. Chen, J. Liu and C. Li, Shallow-layer pillaring of a conductive polymer in monolithic grains to drive superior zinc storage via a cascading effect, *Energy & Environmental Science*, 2020, **13**, 3149-3163.
7. Y. Liu, Y. Jiang, Z. Hu, J. Peng, W. Lai, D. Wu, S. Zuo, J. Zhang, B. Chen, Z. Dai, Y. Yang, Y. Huang, W. Zhang, W. Zhao, W. Zhang, L. Wang and S. Chou, In-Situ Electrochemically Activated Surface Vanadium Valence in V_2C MXene to Achieve High Capacity and Superior Rate Performance for Zn-Ion Batteries, *Advanced Functional Materials*, 2020, **n/a**, 2008033.